Nanoscale

PAPER

View Article Online
View Journal | View Issue

Cite this: *Nanoscale*, 2021, **13**, 4660

A novel electrochemical lung cancer biomarker cytokeratin 19 fragment antigen 21-1 immunosensor based on Si_3N_4/MoS_2 incorporated MWCNTs and core–shell type magnetic nanoparticles†

Mehmet Lütfi Yola, *[a] Necip Atar[b] and Nermin Özcan[c]

Lung cancer is one of deadliest and most life threatening cancer types. Cytokeratin 19 fragment antigen 21-1 (CYFRA 21-1) is a significant biomarker for the diagnosis of non-small cell lung cancer (NSCLC). Due to these reasons, a novel electrochemical immunosensor based on a silicon nitride (Si_3N_4)–molybdenum disulfide (MoS_2) composite on multi-walled carbon nanotubes (Si_3N_4/MoS_2–MWCNTs) as an electrochemical sensor platform and core–shell type magnetic mesoporous silica nanoparticles@gold nanoparticles (MMSNs@AuNPs) as a signal amplifier was presented for CYFRA21-1 detection in this study. Capture antibody (Ab_1) immobilization on a Si_3N_4/MoS_2–MWCNT modified glassy carbon electrode (Si_3N_4/MoS_2–MWCNTs/GCE) was firstly successfully performed by stable electrostatic/ionic interactions between the $-NH_2$ groups of the capture antibody and the polar groups of Si_3N_4/MoS_2. Then, specific antibody–antigen interactions between the electrochemical sensor platform and the signal amplifier formed a novel voltammetric CYFRA21-1 immunosensor. The prepared composite materials and electrochemical sensor surfaces were characterized by transmission electron microscopy (TEM), scanning electron microscopy (SEM), X-ray diffraction (XRD), X-ray photoelectron spectroscopy (XPS), Fourier transform infrared spectroscopy (FTIR), cyclic voltammetry (CV) and electrochemical impedance spectroscopy (EIS). A linearity range of 0.01–1.0 pg mL^{-1} and a low detection limit (LOD) of 2.00 fg mL^{-1} were also obtained for analytical applications. Thus, the proposed immunosensor based on Si_3N_4/MoS_2–MWCNTs and MMSNs@AuNPs has great potential for medical diagnosis of lung cancer.

Received 13th January 2021,
Accepted 2nd February 2021

DOI: 10.1039/d1nr00244a

rsc.li/nanoscale

1. Introduction

Lung cancer is the most common malignant tumor in the world. It is difficult to diagnose in the early period because it usually gives nonspecific findings. Because of this, patients with lung cancer have a high mortality rate.[1] According to the World Health Organization, this rate can be about 90–95%.[2] Lung cancer, which is spreading rapidly in the world, is defined as one of the most common types of cancer after prostate cancer in men and breast cancer in women. Lung cancer, whose most significant cause is shown to be smoking, can manifest itself especially with shortness of breath, wheezing, sudden weight loss or various pains. Thus, a rapid and sensitive diagnosis is significant for patients with lung cancer. The cancer severity directly corresponds to tumor marker levels in the plasma of cancer patients, suggesting that the recognition of these markers has attracted intense interest.[3,4] Cytokeratins are intermediary filaments that form the skeleton of epithelial cells and are divided into different subtypes according to their molecular weights. In general, it can be said that low molecular weight cytokeratins belong to the simple and glandular epithelium, while high molecular weight cytokeratins belong to the multilayer and epidermal type epithelium.[5] Cytokeratin-19 (CK-19) is the lowest molecular weight cytokeratin with a weight of 40 kDa and is found in simple epithelial cells. CYFRA21-1 is a soluble fragment of CK19 and it is released in cells during apoptosis' intermediate stage.[6] In addition, CYFRA21-1 serves as a biomarker in several malignancies.[7] Furthermore, a high expression rate in the plasma of many

[a]*Hasan Kalyoncu University, Faculty of Health Sciences, Department of Nutrition and Dietetics, Gaziantep, Turkey. E-mail: mlutfi.yola@hku.edu.tr; Fax: +903422118081; Tel: +903422118080*
[b]*Pamukkale University, Faculty of Engineering, Department of Chemical Engineering, Denizli, Turkey*
[c]*Iskenderun Technical University, Faculty of Engineering and Natural Sciences, Department of Biomedical Engineering, Hatay, Turkey*
†Electronic supplementary information (ESI) available. See DOI: 10.1039/d1nr00244a

patients with non-small cell lung cancer shows CYFRA21-1's presence.[7] In addition, CYFRA21-1's pre-treatment is importantly related to the stage of disease and its high concentration is a negative prognostic indicator of patients with NSCLC.[8] Thus, the sensitive and selective detection of CYFRA21-1 has started to attract great attention.

Up to now, traditional methods such as fluorometry,[7,9] surface plasmon resonance analysis,[10] and the immunoradiometric assay method[11] have been used for CYFRA21-1 detection. In addition, immunosensors based on voltammetry have been reported for the detection of lung cancer biomarkers.[12,13] These immunosensors have some positive properties such as selectivity, sensitivity and lower costs in comparison with traditional methods.[14,15] In particular, voltammetry has gained attention as an important analytical method used for precision and sensitive detection in recent years.[16–19]

Immunosensors can be designed in two ways such as (i) sandwich-type with a label and (ii) label-free. In particular, sandwich-type immunosensors are frequently used as a result of high sensitivity and stable sensor signals.[20,21] In these sandwich-type immunosensors, after the conjugation of primary antibodies to a sensor platform modified with a nanomaterial/nanocomposite and secondary antibodies likewise to a nanomaterial/nanocomposite surface, the target antigens are sandwiched between primary and secondary antibodies.[22,23] In the literature, significant immunosensors for many different purposes have been reported. For example, a photothermal–thermoelectric coupled immunoassay of α-fetoprotein was performed using Seebeck effect transduction. The developed photothermal–thermoelectric coupled immunosensor demonstrated a LOD of 0.39 ng mL^{-1}.[24] Secondly, MXene quantum dot-encapsulated liposomes for sandwich-type photothermal immunoassay of prostate-specific antigen (PSA) were prepared using a near-infrared camera. An MXene quantum dot-based photothermal immunosensor showed a linearity range from 1.0 ng mL^{-1} to 50 ng mL^{-1} with a LOD of 0.4 ng mL^{-1} for PSA.[25] In another study, a near-IR light-activated non-enzymatic signal-off photoelectrochemical immunosensor for α-fetoprotein analysis was constructed using branched polyethylenimine modified upconversion nanoparticle@CdTe quantum dots. This photoelectrochemical immunosensor showed a linearity range from 10.0 pg mL^{-1} to 50.0 ng mL^{-1} with a LOD of 1.2 pg mL^{-1}.[26] Finally, a paper electrode-based flexible pressure sensor modified with carbon nanotubes was developed for immunoassay of carcinoembryonic antigen with digital multimeter readout. This pressure sensor-based technique showed a linearity range of 0.5–60.0 ng mL^{-1} with a LOD of 167.0 pg mL^{-1}.[27] In addition, some CYFRA 21-1 detections were performed using immunosensor technology. For instance, a photoelectrochemical immunosensor based on $In_2O_3/In_2S_3/CdIn_2S_4$ was developed for CYFRA 21-1 detection.[28] A linearity range of 0.50 pg mL^{-1}–50.0 ng mL^{-1} and a LOD of 0.16 pg mL^{-1} were also obtained. In another study, a label-free electrochemical immunosensor for CYFRA 21-1 recognition based on graphene and AuNPs was prepared and applied to clinical serum samples.[29] A linearity range of 0.25–800 ng mL^{-1} and a low LOD of 100.0 pg mL^{-1} were obtained. The graphene–AuNP composite demonstrated high biological activity and specific surface area in CYFRA 21-1 analysis. Fluorometry based immunosensing for CYFRA 21-1 determination was also presented and a LOD of 0.008 ng mL^{-1} was calculated. A florimetric immunosensor was designed by a hydrothermal method for the preparation of carbon quantum dots using *Citrus lemon* pericarp.[9]

In this study, a novel sandwich-type voltammetric immunosensor based on Si_3N_4/MoS_2–MWCNTs and core–shell type magnetic mesoporous silica nanoparticles@gold nanoparticles for CYFRA 21-1 analysis was developed. Considering the literature in terms of CYFRA 21-1 analysis, it is seen that conventional methods such as fluorometry and surface plasmon resonance analysis have been developed. Nonetheless, these methods have some problems such as high cost equipment, slowness and the need for experienced staff. Thanks to the immunosensor we developed in this study, highly sensitive analysis was performed in a shorter time. The developed immunosensor in this study was prepared using Si_3N_4/MoS_2–MWCNTs and MMSNs@AuNPs. Because the preparation procedures of these composites were low-cost and caused the least waste generation, it is possible to state that an environmentally friendly immunosensor is developed. In addition, the developed immunosensor showed a LOD of 2.00 fg mL^{-1} and perfect selective responses in the presence of other substances in comparison with conventional methods. Hence, the prepared immunosensor can provide a chance in terms of early detection of lung cancer *via* this biosensor.

2. Experimental

2.1. Materials

Cytokeratin fragment antigen 21-1 (CYFRA21-1), CYFRA21-1 primary antibody (anti-CYFRA21-1-Ab_1), CYFRA21-1 secondary antibody (anti-CYFRA21-1-Ab_2), carcinoembryonic antigen (CEA), ascorbic acid (AA), dopamine hydrochloride (DA), uric acid (UA), bovine serum albumin (BSA), sodium sulfide (Na_2S), ammonium heptamolybdate tetrahydrate (AHMT, $(NH_4)_6Mo_7O_{24}$), citric acid (CA, $C_6H_8O_7$), silicon nitride (Si_3N_4), MWCNTs (25–30 nm in diameter and 1.0–5.0 μm in length), dimethylformamide (DMF), cetyltrimethylammonium bromide (CTAB), 3,3′,5,5′-tetramethylbenzidine (TMB), tetraethyl orthosilicate (TEOS), and (3-aminopropyl)triethoxysilane (APTES) were purchased from Sigma-Aldrich. Phosphate buffer solution (PBS, 0.1 M, pH 7.0) as a supporting electrolyte and dilution buffer was also utilized.

2.2. Instrumentation

SEM and XRD images were obtained using a ZEISS EVO 50 SEM analytical microscope and Rigaku X-ray diffractometer, respectively. A JEOL 2100 TEM was used for TEM measurement. XPS analysis was carried out using a PHI 5000 Versa Probe. Gamry Reference 600 work-station (Gamry, USA) was utilized for differential pulse voltammetry (DPV), CV and EIS measurements. FTIR measurements were performed using a Bruker Tensor 27 FT-IR with a DTGS detector.

2.3. Preparation of MoS_2, Si_3N_4/MoS_2 and Si_3N_4/MoS_2–MWCNT composites

The hydrothermal method was performed for MoS_2 synthesis. Na_2S as a sulfur source was utilized in the MoS_2 synthesis process. After the preparation of a mixture of AHMT (1.50 g) and CA (0.50 g) in 25.0 mL distilled water, the dispersion was stirred constantly for 20 min. After that, Na_2S (0.50 g) was added to the above dispersion and the dispersion was mixed with a magnetic stirrer until the green color turned red. In a subsequent experiment, the prepared solution was transferred into a Teflon autoclave at 200 °C for 120 min. After 120 min, the black dispersion was centrifuged at 5000 rpm and washed with distilled water and **MoS_2** was stored at 25 °C.[30]

MoS_2 (250.0 mg) and Si_3N_4 powder (250.0 mg) were transferred to a milling jar. Then, the prepared material was milled for 15 h with a rotating speed of 200 rpm and collected. After that, the material was tagged as **Si_3N_4/MoS_2**. After the preparation of a mixture of MWCNTs (50.0 mg) and Si_3N_4/MoS_2 (10.0 mg) in DMF (100.0 mL), the mixture was sonicated for 90 min and the **Si_3N_4/MoS_2–MWCNT** composite was filtered.

2.4. Si_3N_4/MoS_2–MWCNT composite as an electrochemical sensor platform with anti-CYFRA21-1-Ab_1 and antigen CYFRA21-1 immobilization

A triple electrode system including a glassy carbon electrode (GCE) as an indicator electrode, Ag/AgCl/KCl(sat) as a reference electrode and platinum wire as an auxiliary electrode was utilized for all electrochemical measurements. The cleaning protocol of glassy carbon electrodes was firstly performed according to our previous paper.[31] A Si_3N_4/MoS_2–MWCNT composite modified GCE (Si_3N_4/MoS_2–MWCNTs/GCE) was developed by the dropping of composite dispersion (25.0 μL) on the clean GCE surfaces. Then, the solvent on the Si_3N_4/MoS_2–MWCNT/GCE was removed with an IR lamp.

The anti-CYFRA21-1-Ab_1 immobilization on the Si_3N_4/MoS_2–MWCNT/GCE was successfully performed by stable electrostatic/ionic interactions between the $-NH_2$ groups of anti-CYFRA21-1-Ab_1 (30.0 μL, 50.0 μg mL^{-1}) and the polar groups of Si_3N_4/MoS_2 at 37.0 °C for 30 min, generating **anti-CYFRA21-1-Ab_1/Si_3N_4/MoS_2–MWCNTs/GCE**. Then, BSA (2.0% w/v) was utilized to prevent the non-specific interactions and the anti-CYFRA21-1-Ab_1/Si_3N_4/MoS_2–MWCNT/GCE was immersed in BSA dispersion at 37.0 °C for 30 min. After that, CYFRA21-1 antigens with different concentrations were incubated on the anti-CYFRA21-1-Ab_1/Si_3N_4/MoS_2–MWCNT/GCE at 37.0 °C for 30 min, tagged as **CYFRA21-1/anti-CYFRA21-1-Ab_1/Si_3N_4/MoS_2–MWCNTs/GCE**. Lastly, the developed immunosensor platform based on Si_3N_4/MoS_2–MWCNTs was washed with 0.1 M PBS (pH 7.0) to remove unbound CYFRA21-1 proteins.

2.5. Preparation of MMSNs, MMSNs@AuNPs and conjugation of MMSNs@AuNPs with secondary antibody

After the preparation of 3.0 mol L^{-1} $FeCl_3$ solution in 3.0 mol L^{-1} HCl, Na_2SO_3 solution (2.0 mol L^{-1}, 3.0 mL) was slowly added to $FeCl_3$ solution under stirring. After the color transformation from red to yellow, NH_4OH (100.0 mL, 1.0 mol L^{-1}) was slowly added to the above solution under stirring. After that, oleic acid (200.0 μL) was added and the resulting dispersion was stirred with a magnetic stirrer. Finally, the black precipitate (**Fe_3O_4 NPs**) was dried at 25 °C.

Magnetic mesoporous silica nanoparticles (MMSNs) were prepared by a surfactant-templated seed-mediated growth method.[32] After the addition of Fe_3O_4 NPs in chloroform (1.0 mL, 10.0 mg mL^{-1}) to CTAB (0.10 mol L^{-1}) solution, the ultrasonication treatment was performed to remove chloroform for 45 min. The prepared solution was added to the mixture including 25.0 mL distilled water, ethylene glycol (15.0 mL) and NH_4OH (1.0 mL). After that, incubation was carried out at 60 °C for 20 min. Decane (1.0 mL) and TMB (1.0 mL) were added to the incubated solution and stirred for 90 min for homogenization. Lastly, TEOS (500.0 μL) was slowly added and the resulting reaction was followed for 120 min at 100 °C. After centrifugation at 5000 rpm for 40 min, the prepared **MMSNs** were transferred into NH_4NO_3 solution (50.0 mg in 50.0 mL ethanol) and stirred for 1 h at 70 °C. This treatment was repeated four times and the product was filtered and dried at 50 °C.

Secondly, amino modified MMSNs (MMSNs–NH_2) were prepared.[33] After the preparation of MMSN dispersion (60.0 mg in 30.0 mL ethanol), APTES (200.0 μL) was added to the dispersion and stirred at 80 °C for 18 h. Then, **MMSN–NH_2** was collected with a magnet and washed four times with ethanol. After the prepared MMSN–NH_2 (60.0 mg) was dispersed in distilled water (40.0 mL) by ultrasonication for 40 min; $HAuCl_4$ solution (40.0 mmol L^{-1}) was added to the above dispersion under stirring. Then, $NaBH_4$ (20.0 mL, 0.1 mol L^{-1}) was added and stirred at 100 rpm for 60 min. **MMSNs@AuNPs** were washed with distilled water four times. After the preparation of anti-CYFRA21-1-Ab_2 (30.0 μL, 50.0 μg mL^{-1}), secondary anti-CYFRA21-1-Ab_2 was conjugated to MMSNs@AuNPs *via* amino-gold affinity between anti-CYFRA21-1-Ab_2 and MMSNs@AuNP dispersions at 37.0 °C for 30 min.[34] After centrifugation at 5000 rpm, MMSNs@AuNPs conjugated to anti-CYFRA21-1-Ab_2 (**MMSNs@AuNPs/anti-CYFRA21-1-Ab_2**) was stored in pH 7.0, 0.1 M PBS.

2.6. Electrochemical measurements

Antibody–antigen interactions between MMSNs@AuNPs/anti-CYFRA21-1-Ab_2 and CYFRA21-1/anti-CYFRA21-1-Ab_1/Si_3N_4/MoS_2-MWCNTs/GCE provided an electrochemical CYFRA21-1 immunosensor. The above prepared MMSNs@AuNPs/anti-CYFRA21-1-Ab_2 solution (30.0 μL, 15.0 mg mL^{-1}) was incubated on the CYFRA21-1/anti-CYFRA21-1-Ab_1/Si_3N_4/MoS_2–MWCNT/GCE for the immune reaction of 30 min. Then, the prepared electrochemical immunosensor for CYFRA21-1 antigen's recognition was stored in pH 7.0, 0.1 M PBS (3.0 mL). In order to perform voltammetric measurements, 0.1 M PBS including 1.0 mM H_2O_2 was prepared owing to H_2O_2's usage in medical diagnosis.[35] Before the voltammetric measurements, argon gas (99.999%) was passed to remove dissolved oxygen for 15 min. The voltammograms were recorded without

pressure fluctuations at 25 °C in an enclosed cabinet to prevent from external environmental influences. The preparation procedures are shown in Scheme 1, including Si_3N_4/MoS_2–MWCNTs, MMSNs@AuNPs, the immobilization of the capture antibody, the secondary antibody, and the antigen and the final electrochemical immunosensor development. According to Scheme 1, we can explain the most important purposes of the prepared sensor platform (Si_3N_4/MoS_2–

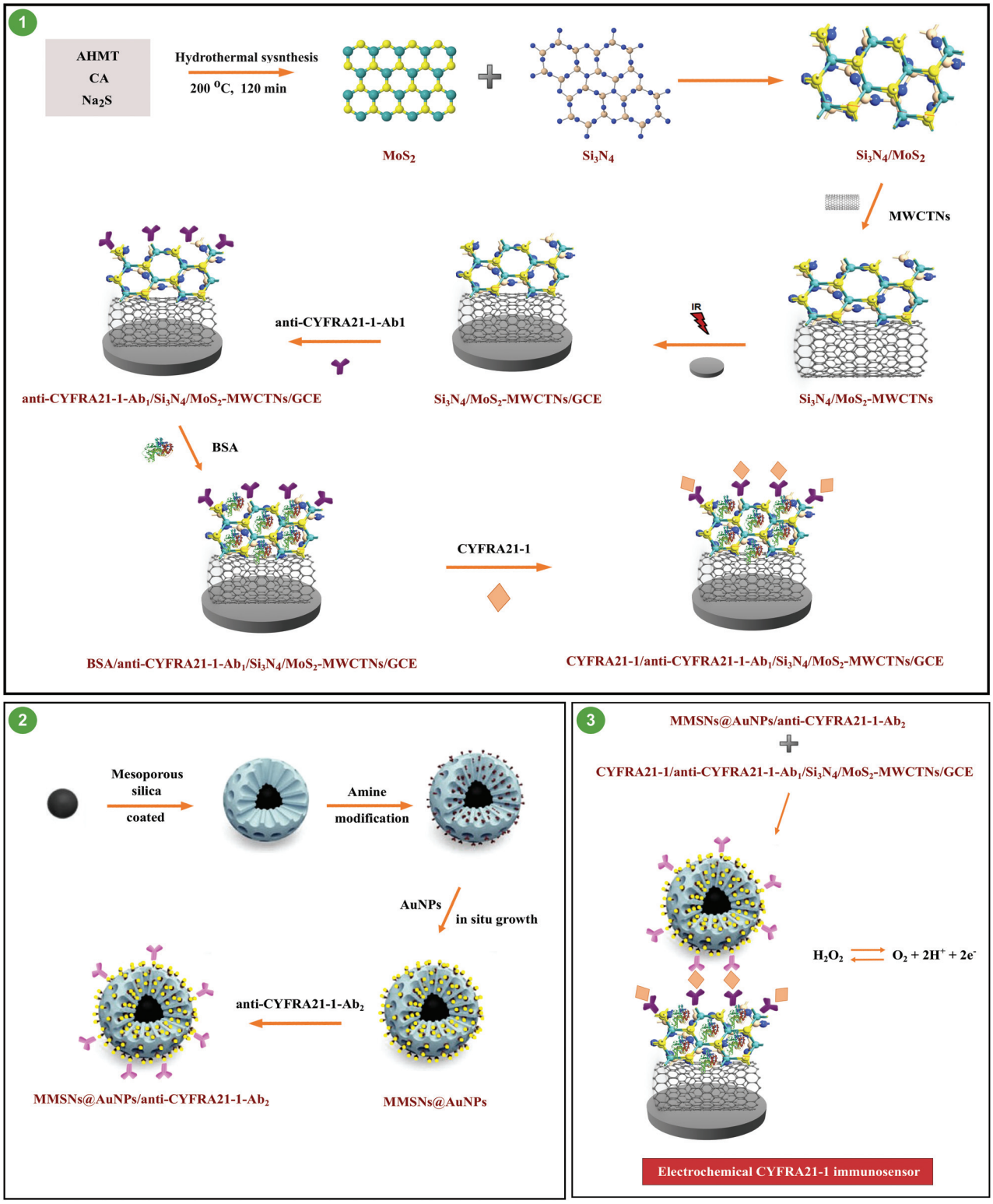

Scheme 1 Preparation procedure of the voltammetric CYFRA21-1 immunosensor.

MWCNTs) as follows: (i) providing anti-CYFRA21-1-Ab_1 immobilization *via* electrostatic/ionic interactions between the $-NH_2$ groups of anti-CYFRA21-1-Ab_1 and the polar groups of Si_3N_4/MoS_2, (ii) providing the increase of surface conductivity *via* MWCNTs. After the conjugation of anti-CYFRA21-1-Ab_2 to the signal amplifier *via* amino-gold affinity, voltammetric measurements were carried out in 0.1 M PBS including 1.0 mM H_2O_2 in the potential range from +0.1 V to +0.5 V. The related electrochemical reaction mechanism for H_2O_2 in the potential range is also provided in Scheme 1 as $\mathbf{H_2O_2 \leftrightarrow O_2 + 2H^+ + 2e^-}$.

2.7. Sample preparation

CYFRA21-1 free plasma samples were supplied from the Blood Bank in Turkey. The sample preparation protocol is explained in detail in the ESI.†[36]

3. Results and discussion

3.1. Characterization of Si_3N_4, MoS_2, Si_3N_4/MoS_2 and the Si_3N_4/MoS_2–MWCNT composite as a sensor platform

Firstly, FTIR measurements were carried out for spectroscopic characterization (Fig. 1A). The obvious two absorption bands attributed to 920 cm^{-1} and 1040 cm^{-1} indicated Si–N group's stretching vibration.[37] For MoS_2, the absorption band at 485 cm^{-1} corresponded to Mo–S's stretching vibration.[38] Lastly, specific bands such as Si–N and Mo–O confirmed the successful synthesis of the Si_3N_4/MoS_2 composite. Then, XRD measurements were performed in the range from 2θ = 10° to 2θ = 80° (Fig. 1B). According to the XRD pattern of Si_3N_4, the diffraction peaks at 2θ = 12.90°, 20.49°, 22.98°, 27.03°, 35.51°, 38.95°, 42.95° and 58.13° were attributed to the (100), (101), (110), (021), (120), (121), (031) and (222) planes, respectively, indicating a hexagonal crystal structure. For MoS_2, the diffraction peaks at 2θ = 13.85°, 33.21°, 40.08° and 59.03° were assigned to the (002), (100), (103) and (110) planes, respectively, indicating a hexagonal crystal structure.[39,40] When we investigate the XRD pattern of the Si_3N_4/MoS_2 composite, the obvious peaks corresponding to Si_3N_4 and MoS_2 were observed for the composite structure. Nonetheless, the peak intensities of the Si_3N_4/MoS_2 composite were lower than that of Si_3N_4, suggesting the structural changes and the decrease in particle size resulting from the milling process. After that, Raman spectroscopy (Fig. 1C), another spectroscopic technique, was used with a 785 nm wavelength laser. In the Raman spectrum of Si_3N_4, the peaks at 255 cm^{-1}, 520 cm^{-1} and 880 cm^{-1} were assigned to silicon nitride's A, Eg, A_{1g} vibrational modes. For MoS_2, the peaks at 370 cm^{-1} and 410 cm^{-1} suggested MoS_2's E^1_{2g} and A^1_g active vibration bands.[30,41] In the Raman spectrum of the Si_3N_4/MoS_2 composite, specific absorption bands belonging to Si_3N_4 and MoS_2 were obtained, and the peak intensities at 255 cm^{-1} and 410 cm^{-1} were lower in comparison with Si_3N_4 and MoS_2. This situation is owing to some surface defects and Si_3N_4/MoS_2 composite formation.

The morphological properties of Si_3N_4, MoS_2 and the Si_3N_4/MoS_2 composite were investigated by SEM (Fig. S1†). The average particle sizes of Si_3N_4, MoS_2 and the Si_3N_4/MoS_2 composite with a polyhedral shape were obtained as about 172 nm, 709 nm and 20 nm, respectively. In addition, the SEM

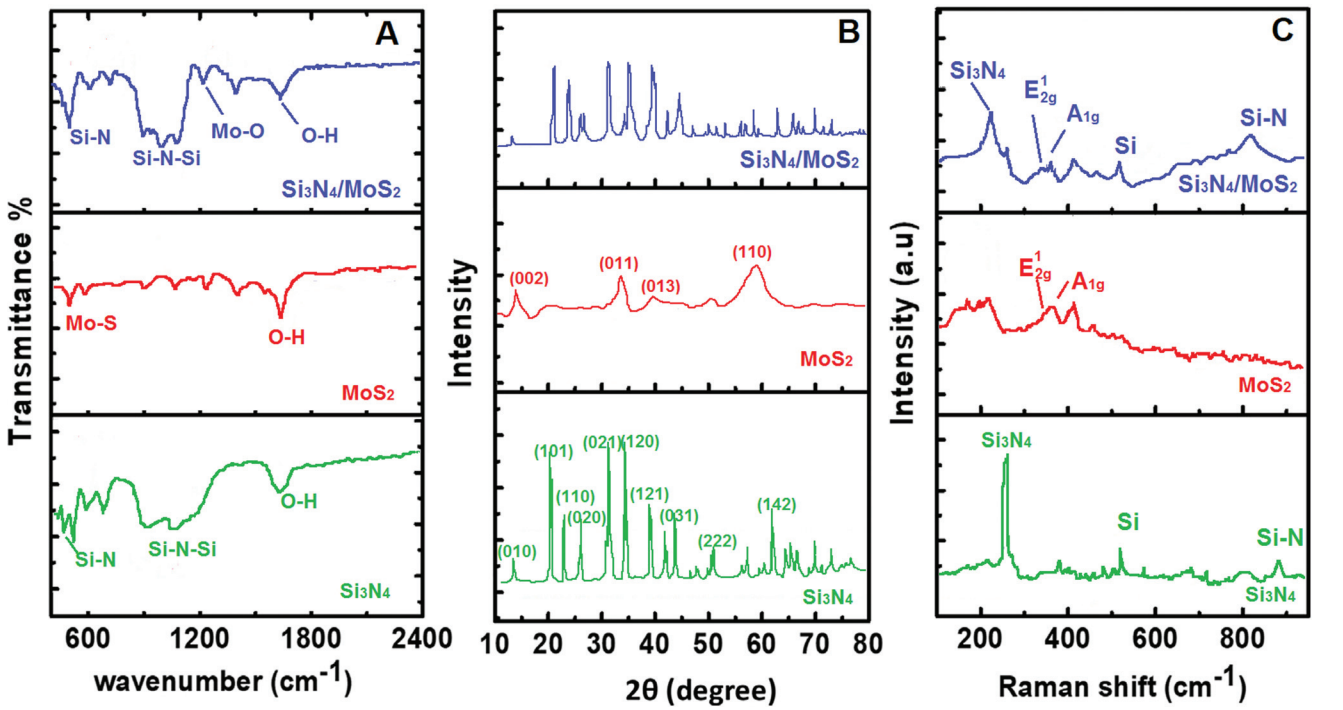

Fig. 1 (A) FTIR spectra, (B) XRD patterns, and (C) Raman spectra of Si_3N_4, MoS_2 and the Si_3N_4/MoS_2 composite.

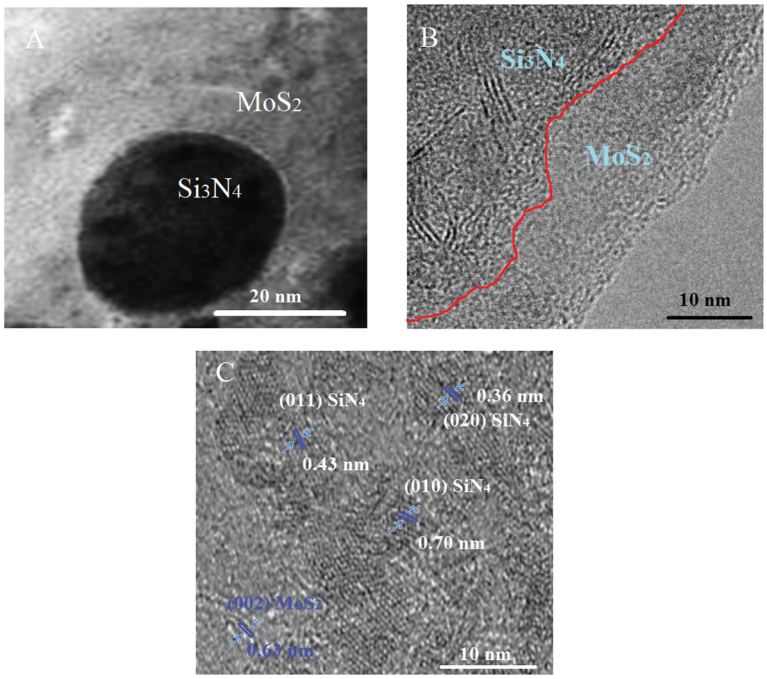

Fig. 2 TEM images (A–C) of the Si_3N_4/MoS_2 composite.

image (Fig. S2A†) of Si_3N_4/MoS_2–MWCNTs showed that Si_3N_4/MoS_2 particles were homogeneously distributed on MWCNTs. Finally, the EDX spectra (Fig. S2B†) of Si_3N_4/MoS_2–MWCNTs were recorded, suggesting the uniform distribution of Si, N, Mo, and S on MWCNTs. Then, the TEM images of the Si_3N_4/MoS_2 composite were obtained (Fig. 2). According to Fig. 2A, the incorporation of Si_3N_4 particles into MoS_2 was successfully realized and the heterojunction interaction occurred between Si_3N_4 and MoS_2 (Fig. 2B). Si_3N_4 particles incorporating MoS_2 were identified from their laminar morphology (Fig. 2C). According to Fig. 2C, lattice spaces such as 0.70, 0.43, and 0.36 nm were attributed to the (010), (011), and (020) planes belonging to Si_3N_4 and 0.63 nm corresponded to the (002) plane belonging to MoS_2.[42]

XPS characterization (Fig. S3†) was performed to show the chemical functionality of the Si_3N_4/MoS_2 composite. According to the Mo 3d high-resolution spectra, the peaks at 231.7 eV (Mo $3d_{3/2}$) and 228.3 eV (Mo $3d_{5/2}$) were attributed to Mo^{4+}'s orbital features. In addition, the peak at 226.3 eV was related to the S 2s interactions in MoS_2.[43] S 2p spectra demonstrated four peaks at 160.36, 162.01, 163.04 and 163.98 eV. The peaks at 162.01 and 163.04 were in harmony with S 2p3/2 and S 2p1/2, confirming S^{2-} of MoS_2.[44] The peak at 163.98 eV was related to the edge sulfur of MoS_2 and a novel peak at 160.36 eV indicated the silicon–sulfur (Si–S) interactions. In the Si 2p spectrum, the peak at 101.6 eV was attributed to the Si^{4+} presence in Si_3N_4.[44] Finally, when we want to investigate the N 1s spectrum, the peaks at 398.12 and 395.22 eV corresponded to nitrogen binding to silicon (N–Si) on Si_3N_4 and the Mo–N interactions, respectively.[45] Thus, the XPS results verified the presence of the Si_3N_4/MoS_2 composite in harmony with Fig. 2. BET measurements of Si_3N_4, Si_3N_4/MoS_2 and Si_3N_4/MoS_2–MWCNTs were performed to show the determination of surface areas (Fig. S4†). Si_3N_4, Si_3N_4/MoS_2 and the Si_3N_4/MoS_2–MWCNT composite showed a type IV adsorption–desorption isotherm. The surface areas of Si_3N_4, Si_3N_4/MoS_2 and Si_3N_4/MoS_2–MWCNTs were calculated as 10.148 $m^2\ g^{-1}$, 16.742 $m^2\ g^{-1}$ and 34.894 $m^2\ g^{-1}$, respectively. Hence, it is concluded that Si_3N_4/MoS_2–MWCNTs with the highest surface area can be used as a sensor platform for effective and greater immobilization of capture antibodies.

3.2. Characterization of Fe_3O_4 NPs, MMSNs and MMSNs@AuNPs

Firstly, TEM characterization was performed for Fe_3O_4 NPs, MMSNs and MMSNs@AuNPs (Fig. 3). Fig. 3A indicates the presence of spherical Fe_3O_4 NPs with the average particle sizes of 25–35 nm. According to Fig. 3B and C, a clear crinkle structure with average particle sizes of 45–50 nm was observed for MMSNs. After AuNP incorporation into MMSNs, the spherical shape of MMSNs appeared to be preserved (Fig. 3D). Fig. 3E confirms the successful incorporation of AuNPs such as the shell formation on MMSNs. Thus, SEM and TEM images confirmed the successful confination of the dispersed AuNPs with a high density by *in situ* $HAuCl_4$ growth on MMSNs. In addition, not only the porous and magnetic mesoporous silicon structure increased the diffusion rate of AuNPs, but also active sites helped in easy immobilization of secondary antibodies. Finally, the EDX image (Fig. 3F) showed the presence of elements such as Fe, O, Si and Au.

Secondly, FTIR characterization was performed for confirmation of the MMSNs and MMSN@AuNP formation

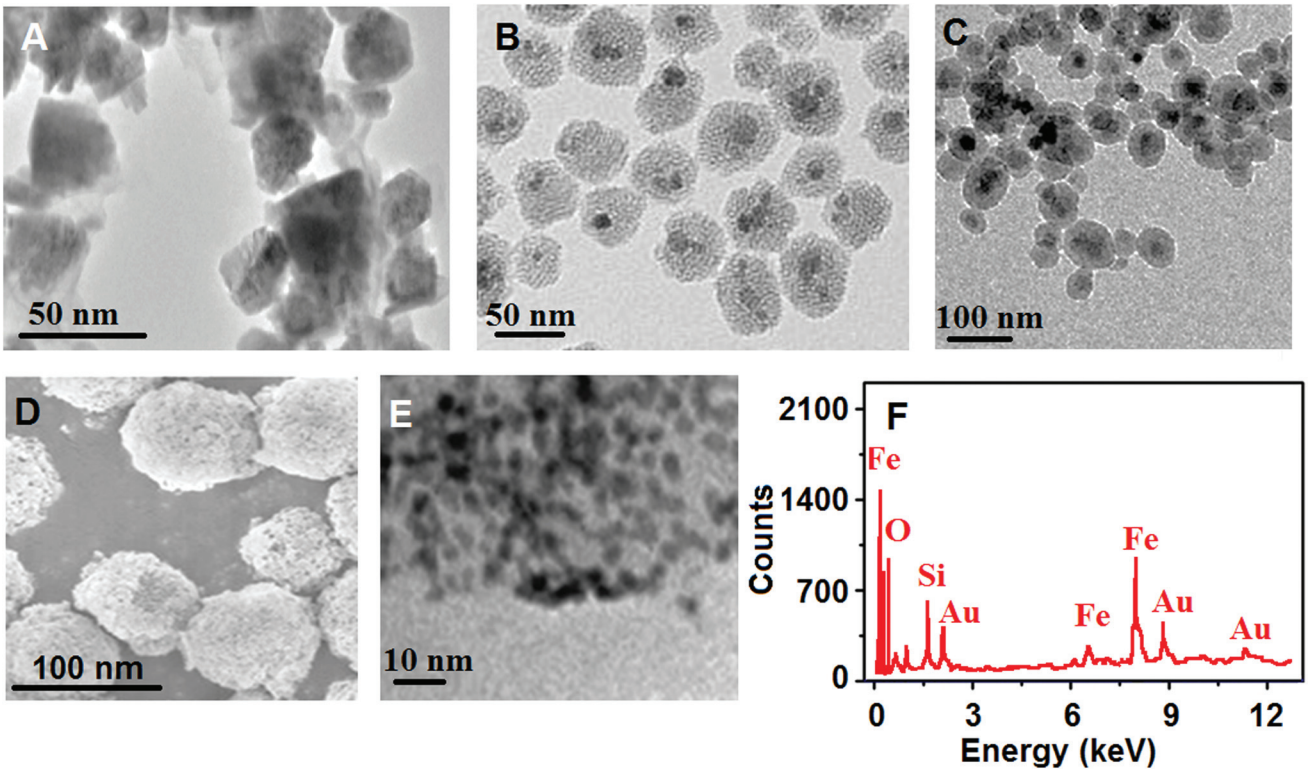

Fig. 3 TEM images of (A) Fe_3O_4 NPs and (B and C) MMSNs, (D) SEM image of MMSNs@AuNPs, (E) HRTEM image of MMSNs@AuNPs, and (F) EDX spectra of MMSNs@AuNPs.

(Fig. S5A†). The specific absorption bands in the range from 582 cm^{-1} to 556 cm^{-1} indicated Fe_3O_4 NPs' coating with mesoporous silicon in the FTIR spectrum of MMSNs. In addition, the absorption bands at 1076 cm^{-1}, 457 cm^{-1} and 928 cm^{-1} corresponded to the stretching Si–O–Si, bending Si–O–Si and bending Si–OH, respectively. The peak at 1557 cm^{-1} in the FTIR spectrum of MMSN–NH_2 corresponded to N–H, indicating the successful modification of MMSNs with amino groups. Thus, we can say that the core–shell type magnetic mesoporous silica nanoparticles@gold nanoparticles were successfully prepared. According to the XRD patterns (Fig. S5B†), the diffraction peaks at 2θ = 29.82°, 36.84°, 42.86°, 57.33° and 62.87° for Fe_3O_4 NPs were assigned to the (220), (222), (400), (511) and (440) planes, respectively. In addition, for MMSNs@AuNPs, the peaks at 2θ = 38.34°, 44.93°, 64.11°, 78.18° and 82.39° were related to the (111), (200), (220), (311) and (222) planes of AuNPs, showing AuNPs' presence on MMSNs. In addition, the XRD pattern of MMSNs@AuNPs demonstrated that the peak intensities in the XRD pattern of Fe_3O_4 NPs decreased with the formation of MMSNs. Thus, these results showed that MMSNs@AuNPs were successfully prepared. Finally, XPS measurements were performed for confirmation of MMSNs@AuNPs (Fig. S5C†). The Fe 2p region was highlighted by Fe 2p1/2 and Fe 2p3/2, appearing at 721.8 and 719.2 eV, respectively. Hence, the Fe_3O_4 NP presence was verified in the Fe 2p region. For the Au 4f narrow region, the peaks at 82.4 and 87.1 eV confirmed AuNPs' formation on MMSNs. Lastly, a large peak at 103.1 eV for Si 2p showed silicon's presence on MMSNs@AuNPs.

3.3. Electrochemical characterization of the proposed voltammetric immunosensor

Electrochemical characterization of the modified sensor platform (CYFRA21-1/anti-CYFRA21-1-Ab_1/Si_3N_4/MoS_2–MWCNTs/GCE) was progressively investigated in 1.0 mM $[Fe(CN)_6]^{3-}$ containing 0.1 M KCl by CV and EIS. A bare GCE demonstrated small anodic and cathodic peak signals in 1.0 mM $[Fe(CN)_6]^{3-}$ (curve a of Fig. S6A†). The more anodic and cathodic peak signals were observed in the MWCNTs/GCE due to the enhanced electrical conductivity on the electrode surface[46] (curve b of Fig. S6A†). Because of the hetero-structured Si_3N_4/MoS_2 providing more active centers and easy electron transfer on MWCNTs (curve c of Fig. S6A†), an increased electrochemical activity was obtained by Si_3N_4/MoS_2–MWCNTs/GCE.[47] After anti-CYFRA21-1-Ab_1 immobilization on the Si_3N_4/MoS_2–MWCNTs/GCE by electrostatic/ionic interactions, the anodic and cathodic peak intensities decreased in comparison with curve c, suggesting the successful anti-CYFRA21-1-Ab_1 immobilization (curve d of Fig. S6A†). After the sequential immobilization treatments of BSA and CYFRA21-1 antigens, the anodic and cathodic peak signals further decreased (curve e and f of Fig. S6A†). Hence, the obstructive effect on electron transfer started to become more noticeable. Hence, the successful attachments of primary, secondary and antigen pro-

teins to the electrode surface were observed from the CV results.

Then, EIS measurements were performed in 1.0 mM $[Fe(CN)_6]^{3-}$ containing 0.1 M KCl to confirm the CV results (Fig. S6B†). The EIS graph of the bare GCE was shown in curve a of Fig. S6B.† When the resistance values were investigated on MWCNT/GCE (curve b of Fig. S6B†) and Si_3N_4/MoS_2–MWCNT/GCE (curve c of Fig. S6B†), the values gradually reduced, suggesting that the electron transfer occurred more easily in harmony with the CV results. After anti-CYFRA21-1-Ab_1 immobilization on Si_3N_4/MoS_2–MWCNTs/GCE, the resistance values on the electrode surface appeared to be higher (curve d of Fig. S6B†). According to curves e and f of Fig. S6B,† the blocking effect on electron transfer was in harmony with Fig. S6A.† Hence, the successful immunosensor construction was presented for CYFRA21-1 recognition.

In addition, several immunosensors including AuNPs/anti-CYFRA21-1-Ab_2 and MMSNs@AuNPs/anti-CYFRA21-1-Ab_2 were developed to observe the effect of signal amplification (Fig. S6C†). First of all, the sensor platforms (Si_3N_4/MoS_2–MWCNTs/GCE) including anti-CYFRA21-1-Ab_1 and antigen CYFRA21-1 were subjected to an immune reaction for 30 min with MMSNs@AuNPs/anti-CYFRA21-1-Ab_2, AuNPs/anti-CYFRA21-1-Ab_2 and anti-CYFRA21-1-Ab_2, respectively. Then, all immunosensors were tested in 1.0 mM H_2O_2 in pH 7.0, 0.1 M PBS and in the absence of H_2O_2. H_2O_2 as a redox probe was selected due to its use in biomolecules' medical diagnosis.[35] H_2O_2 oxidation into O_2 at about +0.30 V was followed using the above voltammetric immunosensors. The signal amplifier containing only anti-CYFRA21-1-Ab_2 showed a small signal (about 2.0 μA) for 1.0 mM H_2O_2 (curve b of Fig. S6C†). When we used AuNPs/anti-CYFRA21-1-Ab_2 (curve c of Fig. S6C†) and MMSNs@AuNPs/anti-CYFRA21-1-Ab_2 (curve d of Fig. S6C†) for immunosensor development, peak signals corresponding to 8.0 μA and 13.0 μA were obtained, respectively. Due to the high specific surface area and good electrical conductivity of AuNPs,[48,49] an enhanced electrochemical activity was observed in comparison with curve b of Fig. S6C.† Furthermore, owing to the synergistic effect providing a larger surface area between AuNPs and MMSNs,[50,51] the anti-CYFRA21-1-Ab_2 conjugation process was realized more efficiently on MMSNs@AuNPs. Thus, we selected MMSNs@AuNPs/anti-CYFRA21-1-Ab_2 signal amplification for subsequent immunosensor application.

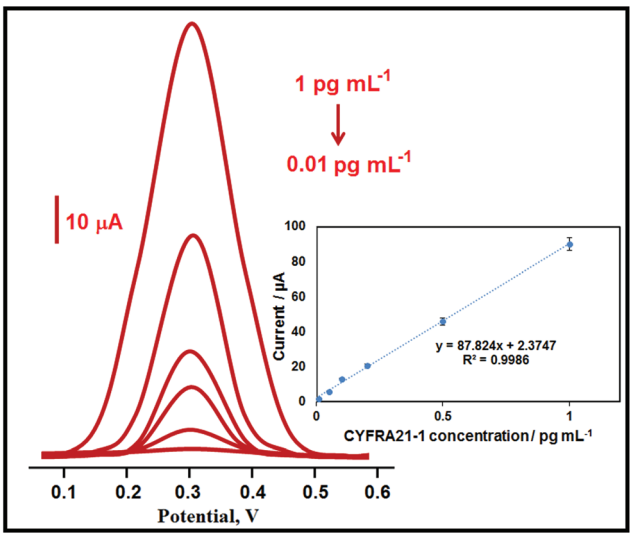

Fig. 4 Concentration effect (from 0.01 to 1.0 pg ml^{-1} CYFRA21-1) on immunosensor signals, inset: the calibration curve for the voltammetric CYFRA21-1 immunosensor.

3.4. Optimization for voltammetric measurements

The effects of pH, immune reaction time, H_2O_2 and MMSNs@AuNPs/anti-CYFRA21-1-Ab_2 solution concentrations were evaluated in detail in Fig. S7.†

3.5. Linearity range

Fig. 4 demonstrates differential pulse voltammograms with concentration increase and the obtained linearity was found to be y (μA) = 87.824x (pg mL^{-1}) + 2.3747 (inset of Fig. 4). The quantification limit (LOQ) and LOD were calculated as 0.01 pg mL^{-1} and 2.00 fg mL^{-1}, respectively using eqn (1) and (2) below:

$$\mathrm{LOQ} = 10.0S/m \quad (1)$$

$$\mathrm{LOD} = 3.3S/m \quad (2)$$

where S is the standard deviation of intercept and m is the slope of the calibration equation. Table 1 shows the comparative work between the voltammetric CYFRA21-1 immunosensor and the other analytical methods. The prepared immunosensor suggested a low LOD, confirming that this biosensor quantifies the CYFRA21-1 concentration with high selectivity. This

Table 1 Comparison of the voltammetric CYFRA21-1 immunosensor with other techniques

Material/method	Linearity ranges	LOD	Ref.
Graphene@gold nanoparticles	0.25–800.0 ng mL^{-1}	100.0 pg mL^{-1}	29
APTES/ZrO_2–RGO/ITO	2.00–22.0 ng mL^{-1}	0.12 ng mL^{-1}	52
QPs-LFTS	1.30–480.0 ng mL^{-1}	0.16 ng mL^{-1}	53
CdSe/ZnS quantum dots	0.50–128.0 ng mL^{-1}	0.20 ng mL^{-1}	54
Poly(thionine)–Au composite	0.50 ng mL^{-1}–10.0 fg mL^{-1}	4.60 fg mL^{-1}	55
Polydopamine/tungsten oxide nanocomposite	0.50 pg mL^{-1}–10.0 ng mL^{-1}	2.50 fg mL^{-1}	56
AuNPs/amperometry	50.0 fg mL^{-1}–100.0 ng mL^{-1}	38.0 fg mL^{-1}	57
MMSNs@AuNPs	**0.01–1.0 pg mL^{-1}**	**2.0 fg mL^{-1}**	**This study**

performance resulted from the high surface area, good electrical conductivity and synergistic effect between AuNPs and MMSNs, providing many binding sites for the antigen and antibody. In addition, the preparation procedures of Si_3N_4/MoS_2–MWCNTs and MMSNs@AuNPs were low-cost and the least waste generation occurred, presenting an environmentally friendly immunosensor.

3.6. Recovery

Firstly, recovery experiments were performed to show the voltammetric CYFRA21-1 immunosensor's high selectivity. The recovery was calculated using eqn (3) below:

$$\text{Recovery} = \frac{\text{found CYFRA21-1, pg mL}^{-1}}{\text{real CYFRA21-1, pg mL}^{-1}} \quad (3)$$

The close values to 100.00% (Table S1†) confirmed the voltammetric CYFRA21-1 immunosensor's high selectivity. Furthermore, the standard addition method was applied to prepare plasma samples (sample preparation in the ESI†) to verify the immunosensor's high selectivity. The obtained calibration equation by the standard addition method was y (μA) = 87.843x (pg mL^{-1}) + 10.1791. The close slope values between direct calibration and standard addition methods showed that this biosensor can quantify the CYFRA21-1 concentration with high selectivity without the interference effect in plasma medium.

3.7. Selectivity, stability, reproducibility and reusability

For selectivity test, 6 different protein solution mixtures were prepared: (i) 0.100 pg mL^{-1} CYFRA21-1, (ii) 0.100 pg mL^{-1} CYFRA21-1 + 10.00 pg mL^{-1} CEA, (iii) 0.100 pg mL^{-1} CYFRA21-1 + 10.00 pg mL^{-1} AA, (iv) 0.100 pg mL^{-1} CYFRA21-1 + 10.00 pg mL^{-1} DA, (v) 0.100 pg mL^{-1} CYFRA21-1 + 10.00 pg mL^{-1} UA, (vi) 0.100 pg mL^{-1} CYFRA21-1 + 10.00 pg mL^{-1} BSA. After that, 6 different voltammetric CYFRA21-1 immunosensors were separately developed using these 6 antigen protein solutions according to section 2.5 and section 2.6. The prepared 6 immunosensors were applied to 1.0 mM H_2O_2 solution including in pH 7.0, 0.1 M PBS. According to Fig. S8A,† 0.34% of relative standard deviation (RSD) showed a high selectivity of the voltammetric CYFRA21-1 immunosensor.

The stability of one voltammetric CYFRA21-1 immunosensor was investigated in a 4 °C storage environment for seven weeks. The observed signals during seven weeks were about 98.61% of the first current signal (Fig. S8B†). Thus, a voltammetric CYFRA21-1 immunosensor with high stability was presented for clinical applications.

For the reproducibility test, 10 voltammetric CYFRA21-1 immunosensors having 0.100 pg mL^{-1} CYFRA21-1 were independently prepared according to sections 2.5, 2.4 and 2.6 and used towards 1.0 mM H_2O_2 solution. 0.27% of RSD confirmed the high reliability of the immunosensor production procedure.

Finally, the reusability of the voltammetric CYFRA21-1 immunosensor was investigated. The current signals were constantly recorded during 25 times usage of only one prepared CYFRA21-1 immunosensor and the RSD value of the recorded current signals was obtained as 0.15%. Hence, a voltammetric CYFRA21-1 immunosensor with a high degree of reusability was prepared in the present study.

3.8. Precision and accuracy

Three concentrations (0.100, 0.200 and 0.500 pg mL^{-1} CYFRA21-1) in the linearity range were determined on the same day (intra-day precision) and six consecutive days (inter-day precision) (Table S2†). The calculated RSD values were 0.049–0.366 for intra-day and 0.098–0.485 for inter-day precision. Therefore, a low RSD demonstrated high precision of the voltammetric CYFRA21-1 immunosensor. Accuracy was investigated as % relative error between the found and added concentrations for CYFRA21-1 (Bias %). Hence, low Bias % (Table S2†) confirmed that the accuracy of the voltammetric CYFRA21-1 immunosensor was high.

4. Conclusions

In this study, a selective, sensitive, stable and reproducible new-type voltammetric immunosensor based on a silicon nitride (Si_3N_4)–molybdenum disulfide (MoS_2) composite on multi-walled carbon nanotubes (Si_3N_4/MoS_2–MWCNTs) as an electrochemical sensor platform and core–shell type magnetic mesoporous silica nanoparticles@gold nanoparticles (MMSNs@AuNPs) as a signal amplifier were prepared and applied to cytokeratin 19 fragment antigen 21-1 detection in plasma samples. The prepared CYFRA21-1 biosensor had a more satisfactory sensitivity and showed a lower detection limit of 2.0 fg mL^{-1} in comparison with other detection methods. Thus, the development of an environmentally friendly immunosensor offers an alternative biosensor for clinical diagnosis.

Conflicts of interest

There are no conflicts of interest to declare.

Acknowledgements

Mehmet Lütfi YOLA would like to thank the Turkish Academy of Sciences (TUBA- GEBIP) for their invaluable support.

References

1 M. Chen, C. Hou, D. Huo, M. Yang and H. Fa, *Anal. Methods*, 2015, **7**, 9466–9473.
2 L. Wang, N. Liu and Z. Ma, *J. Mater. Chem. B*, 2015, **3**, 2867–2872.
3 F. Yang, J. Han, Y. Zhuo, Z. Yang, Y. Chai and R. Yuan, *Biosens. Bioelectron.*, 2014, **55**, 360–365.
4 S. Holdenrieder, B. Wehnl, K. Hettwer, K. Simon, S. Uhlig and F. Dayyani, *Br. J. Cancer*, 2017, **116**, 1037–1045.

5 Z. W. Baloch, S. Abraham, S. Roberts and V. A. LiVolsi, *Hum. Pathol.*, 1999, **30**, 1166–1171.
6 H.-H. Wu, P.-H. Wang, J.-Y. Yeh, Y.-J. Chen, M.-S. Yen, R.-L. Huang, Y.-J. Tsai and C.-C. Yuan, *Taiwan. J. Obstet. Gynecol.*, 2014, **53**, 30–34.
7 S. Boeck, C. Wittwer, V. Heinemann, M. Haas, C. Kern, P. Stieber, D. Nagel and S. Holdenrieder, *Br. J. Cancer*, 2013, **108**, 1684–1694.
8 Y. Xu, L. Xu, M. Qiu, J. Wang, Q. Zhou, L. Xu, J. Wang and R. Yin, *Sci. Rep.*, 2015, **5**, 1–10.
9 N. A. Alarfaj, M. F. El-Tohamy and H. F. Oraby, *Nanoscale Res. Lett.*, 2020, **15**, 12.
10 N. F. Chiu and H. T. Yang, *Front. Bioeng. Biotechnol.*, 2020, **8**, 234.
11 B. Nakata, T. Takashima, Y. Ogawa, T. Ishikawa and K. Hirakawa, *Br. J. Cancer*, 2004, **91**, 873–878.
12 H. Yang, J. Bao, D. Huo, Y. Zeng, X. Wang, M. Samalo, J. Zhao, S. Zhang, C. Shen and C. Hou, *Talanta*, 2021, **224**, 121816.
13 A. Khanmohammadi, A. Aghaie, E. Vahedi, A. Qazvini, M. Ghanei, A. Afkhami, A. Hajian and H. Bagheri, *Talanta*, 2020, **206**, 120251.
14 H.-H. Jeong, N. Erdene, J.-H. Park, D.-H. Jeong, H.-Y. Lee and S.-K. Lee, *Biosens. Bioelectron.*, 2013, **39**, 346–351.
15 X. Luo and J. J. Davis, *Chem. Soc. Rev.*, 2013, **42**, 5944–5962.
16 H. Karimi-Maleh, F. Karimi, S. Malekmohammadi, N. Zakariae, R. Esmaeili, S. Rostamnia, M. L. Yola, N. Atar, S. Movaghgharnezhad and S. Rajendran, *J. Mol. Liq.*, 2020, **310**, 113185.
17 H. Karimi-Maleh and O. A. Arotiba, *J. Colloid Interface Sci.*, 2020, **560**, 208–212.
18 H. Karimi-Maleh, F. Karimi, M. Alizadeh and A. L. Sanati, *Chem. Rec.*, 2020, **20**, 682–692.
19 H. Karimi-Maleh, M. Sheikhshoaie, I. Sheikhshoaie, M. Ranjbar, J. Alizadeh, N. W. Maxakato and A. Abbaspourrad, *New J. Chem.*, 2019, **43**, 2362–2367.
20 H. Medetalibeyoglu, M. Beytur, O. Akyıldırım, N. Atar and M. L. Yola, *Sens. Actuators, B*, 2020, **319**, 128195.
21 X. Pei, B. Zhang, J. Tang, B. Liu, W. Lai and D. Tang, *Anal. Chim. Acta*, 2013, **758**, 1–18.
22 M. L. Yola and N. Atar, *Nanoscale*, 2020, **12**, 19824–19832.
23 S. Lv, K. Zhang, L. Zhu and D. Tang, *Anal. Chem.*, 2019, **92**, 1470–1476.
24 L. Huang, J. Chen, Z. Yu and D. Tang, *Anal. Chem.*, 2020, **92**, 2809–2814.
25 G. Cai, Z. Yu, P. Tong and D. Tang, *Nanoscale*, 2019, **11**, 15659–15667.
26 Z. Luo, Q. Qi, L. Zhang, R. Zeng, L. Su and D. Tang, *Anal. Chem.*, 2019, **91**, 4149–4156.
27 Z. Yu, Y. Tang, G. Cai, R. Ren and D. Tang, *Anal. Chem.*, 2018, **91**, 1222–1226.
28 T. Wu, J. Feng, S. Zhang, L. Liu, X. Ren, D. Fan, X. Kuang, X. Sun, Q. Wei and H. Ju, *Biosens. Bioelectron.*, 2020, **169**, 112580.
29 Y. Zeng, J. Bao, Y. Zhao, D. Huo, M. Chen, M. Yang, H. Fa and C. Hou, *Talanta*, 2018, **178**, 122–128.
30 G. Nagaraju, C. N. Tharamani, G. T. Chandrappa and J. Livage, *Nanoscale Res. Lett.*, 2007, **2**, 461.
31 M. L. Yola and N. Atar, *Mater. Sci. Eng., C*, 2019, **96**, 669–676.
32 S. Angelos, N. M. Khashab, Y.-W. Yang, A. Trabolsi, H. A. Khatib, J. F. Stoddart and J. I. Zink, *J. Am. Chem. Soc.*, 2009, **131**, 12912–12914.
33 W. Luo, C. Zhu, S. Su, D. Li, Y. He, Q. Huang and C. Fan, *ACS Nano*, 2010, **4**, 7451–7458.
34 B. Đ. Glišić, U. Rychlewska and M. I. Djuran, *Dalton Trans.*, 2012, **41**, 6887–6901.
35 V. Stanković, S. Đurđić, M. Ognjanović, J. Mutić, K. Kalcher and D. M. Stanković, *J. Electroanal. Chem.*, 2020, **876**, 114487.
36 M. L. Yola and N. Atar, *Biosens. Bioelectron.*, 2019, **126**, 418–424.
37 K. Sardar, R. Bounds, M. Carravetta, G. Cutts, J. S. J. Hargreaves, A. L. Hector, J. A. Hriljac, W. Levason and F. Wilson, *Dalton Trans.*, 2016, **45**, 5765–5774.
38 A. S. Krishna Kumar, S.-J. Jiang and J. K. Warchoł, *ACS Omega*, 2017, **2**, 6187–6200.
39 D. Duphil, S. Bastide and C. Lévy-Clément, *J. Mater. Chem.*, 2002, **12**, 2430–2432.
40 H. Yu, Y. Liu and S. L. Brock, *Inorg. Chem.*, 2008, **47**, 1428–1434.
41 H. Zhao, Y. Dong, P. Jiang, H. Miao, G. Wang and J. Zhang, *J. Mater. Chem. A*, 2015, **3**, 7375–7381.
42 K. D. Rasamani, F. Alimohammadi and Y. Sun, *Mater. Today*, 2017, **20**, 83–91.
43 D. Ganta, S. Sinha and R. T. Haasch, *Surf. Sci. Spectra*, 2014, **21**, 19–27.
44 A. Rauf, M. S. A. Sher Shah, G. H. Choi, U. B. Humayoun, D. H. Yoon, J. W. Bae, J. Park, W.-J. Kim and P. J. Yoo, *ACS Sustainable Chem. Eng.*, 2015, **3**, 2847–2855.
45 X. D. Huang, X. F. Gan, F. Zhang, Q. A. Huang and J. Z. Yang, *Electrochim. Acta*, 2018, **268**, 241–247.
46 M. L. Yola and N. Atar, *Electrochim. Acta*, 2014, **119**, 24–31.
47 G. Angamuthu, D. Bosubabu, K. Ramesha and V. Rengarajan, *Appl. Mater. Today*, 2021, **22**, 100916.
48 Y. Zhao, D. Huo, J. Bao, M. Yang, M. Chen, J. Hou, H. Fa and C. Hou, *Sens. Actuators, B*, 2017, **244**, 1037–1044.
49 Y. Ge, J. Wu, H. Ju and S. Wu, *Talanta*, 2014, **120**, 218–223.
50 S. Wang, M. Zhang and W. Zhang, *ACS Catal.*, 2011, **1**, 207–211.
51 Y. Lin, Z. Li, Z. Chen, J. Ren and X. Qu, *Biomaterials*, 2013, **34**, 2600–2610.
52 S. Kumar, J. G. Sharma, S. Maji and B. D. Malhotra, *Biosens. Bioelectron.*, 2016, **78**, 497–504.
53 Z. Chen, R. Liang, X. Guo, J. Liang, Q. Deng, M. Li, T. An, T. Liu and Y. Wu, *Biosens. Bioelectron.*, 2017, **91**, 60–65.
54 L. Ding, X. Chen, L. He, F. Yu, S. Yu, J. Wang, Y. Tian, Y. Wang, Y. Wu, L.-E. Liu and L. Qu, *Microchim. Acta*, 2020, **187**, 171.
55 H. Wang, X. Gao and Z. Ma, *Sci. Rep.*, 2017, **7**, 1023.
56 R. Atchudan, N. Muthuchamy, T. Edison, S. Perumal, R. Vinodh, K. H. Park and Y. R. Lee, *Biosens. Bioelectron.*, 2019, **126**, 160–169.
57 H. Wang and Z. Ma, *Microchim. Acta*, 2017, **184**, 1045–1050.